

Geophysical Research Letters[®]



RESEARCH LETTER

10.1029/2021GL095722

Key Points:

- Measurements of Lagrangian and Eulerian velocities are combined with pressure sensor data to explore wave properties in the surf zone
- Wave-by-wave oscillations of mean-water level exert a strong influence on mass transport in the fluid column
- The motion of Lagrangian tracers is well matched by dispersive long-wave theory

Correspondence to:

H. Kalisch,
henrik.kalisch@uib.no

Citation:

Bjørnstad, M., Buckley, M., Kalisch, H., Streßer, M., Horstmann, J., Frøysa, H. G., et al. (2021). Lagrangian measurements of orbital velocities in the surf zone. *Geophysical Research Letters*, 48, e2021GL095722. <https://doi.org/10.1029/2021GL095722>

Received 19 AUG 2021
Accepted 10 OCT 2021

Lagrangian Measurements of Orbital Velocities in the Surf Zone

M. Bjørnstad¹, M. Buckley², H. Kalisch¹ , M. Streßer², J. Horstmann², H. G. Frøysa¹, O. E. Ige¹, M. Cysewski², and R. Carrasco-Alvarez² 

¹Department of Mathematics, University of Bergen, Bergen, Norway, ²Institute of Coastal Ocean Dynamics, Helmholtz-Zentrum Hereon, Geesthacht, Germany

Abstract Eulerian and Lagrangian measurements of orbital velocities in waves approaching a beach are analyzed with the goal of understanding the relative influence of wave-by-wave variations in mean-water level, wave height and incipient wave breaking on mass transport properties of waves in the surf zone. It is shown quantitatively that elevated local mean-water level correlates positively with increased Lagrangian mass transport at the free surface. Eulerian ADV measurements in the fluid column suggest that the depth-integrated wave-by-wave mass transport also correlates positively with the local mean-water level, and is only weakly linked to wave height and wave-breaking events.

Plain Language Summary A sea state is defined broadly by an average wave period and an average perceived (significant) wave height, but wave heights and periods of individual waves may differ significantly from these average values. The differences between individual waves are exacerbated as the waves approach the shore and interact with the bottom topography in shallow water. In particular, the mean-water level may vary from wave to wave. In the present study, particle tracers are used in connection with stereo imaging to study particle trajectories in waves approaching a beach. Particle positions and trajectories are found using data analysis of individual camera frames. In addition, fluid velocities are measured directly using acoustic Doppler velocimetry. It is found that the most significant factor in the overall horizontal fluid velocity and net transport of particles by an individual wave toward the beach is not the wave height or period, but the local mean-water level, that is how the average wave elevation in a single wave is situated with respect to the sea bed.

1. Introduction

Mass transport induced by wave motion is a major factor in the formation of circulation patterns in the nearshore zone which in turn affect beach erosion and resedimentation (Inman & Brush, 1973; Masselink et al., 2014). It is generally thought that the main cause of nearshore circulation are energetic breaking waves which can lead to significant nearshore wave set-up (increased mean-water level) and in connection with bathymetric features lead to undertow, edge waves, and rip currents (Castelle et al., 2016; Davidson-Arnott et al., 2019; Longuet-Higgins & Stewart, 1964; Putrevu & Svendsen, 1999; Svendsen, 2006). It is also well known that localized variations in the mean-water level may develop in nonbreaking waves through self-modulation of wave groups (Longuet-Higgins & Stewart, 1962), leading to *bound* infragravity waves which propagate in sync with the wave group. In bound infragravity waves, the trough of the envelope is generally aligned with a wave set-up (higher mean-water level), while the crest of the envelope is aligned with a wave set-down (Longuet-Higgins & Stewart, 1962). During the shoaling process, the alignment of the crests may change, and a phase shift between the wave group and the corresponding wave envelope may develop (Battjes et al., 2004; Inch et al., 2017; Janssen et al., 2003; List, 1992; Masselink, 1995). In addition, wave set-down through shoaling and the subsequent wave set-up in breaking waves may create low-frequency waves propagating seaward from the surf zone (Buckley et al., 2018; Longuet-Higgins & Stewart, 1964; Tucker, 1950).

Oscillations of the mean-water level at frequencies below the gravity-wave band are known to be important for a number of coastal processes such as beach and dune erosion (Russell, 1993; van Thiel de Vries et al., 2008) and can influence wave set-up, the structure of rip currents and storm surges (Castelle

© 2021. The Authors.

This is an open access article under the terms of the [Creative Commons Attribution License](https://creativecommons.org/licenses/by/4.0/), which permits use, distribution and reproduction in any medium, provided the original work is properly cited.

et al., 2016). Recent field studies also suggest the existence of low-frequency oscillations in currents (Elgar & Raubenheimer, 2020) in the surf zone.

In recent work, the authors of Calvert et al. (2019) showed how set-down in wave groups affect the orbital velocities in the fluid column. The main purpose of the present study is to highlight how oscillations in the mean-water level influence kinematic flow properties of waves and mass transport in the fluid column under field conditions. As opposed to time-averaged measurements over long periods, such as used, for example, in studies of sand transport (see Russell, 1993; De Bakker, Brinkkemper, et al., 2016 and many other studies), in the present study measurements of instantaneous velocities are more appropriate as this allows us to study flow properties featured by *individual* waves in the surf zone. While laboratory studies in shallow water have confirmed some theoretical predictions about infragravity wave formation and shoaling (Lin & Hwung, 2012) as well as particle motion in gravity waves (Chen et al., 2010; Umeyama, 2012) and wave groups (Calvert et al., 2019), wave-by-wave properties of orbital velocities and mass transport remain largely unexplored in the field.

In order to illuminate the details of flow properties in individual waves under field conditions, a measurement campaign was conducted at a beach on the island of Sylt, located off the German North Sea Coast near the border with Denmark. Wave poles with graduation were mounted at low tide, together with pressure sensors (PG) and an acoustic Doppler velocimeter (ADV). In addition, oranges were used as surface tracers in connection with a two-camera stereo imaging system which was able to track the surface tracers. According to Sharifi et al. (2007), oranges are slightly buoyant, and are about 97% submerged in seawater. As a result, they are only marginally affected by wind drag while at the same time being easily visible due to their orange color. Moreover, these tracers are naturally bio-degradable.

Analysis of the measurements showed strong variation in mean-water level between consecutive waves. A spectral analysis revealed that the infragravity signal had a well-defined peak at 28.6 s and a smaller sideband at 13.8 s, and bound infragravity waves were present. As will be laid out presently, the changes in mean-water level from one wave to the next have major implications on the underlying fluid flow. Indeed, the local mean-water level has a pronounced effect on the orbital velocities in the fluid, and an elevated mean-water level leads to strong mass transport both at the free surface and also in the fluid column. In particular, it will be shown that the wave-by-wave variations in the mean-water level have a stronger effect on flow properties in individual waves than changes in the wave height or even the commencement of wave breaking.

2. Field Measurements

The main measurement system in this study was a two-camera stereo imaging system, that was able to resolve the motions of buoyant surface tracers (oranges) at the wavy water surface within the surf zone. Additional supporting wind and wave data were obtained from a combination of both in situ and remote sensing measurement systems, including bottom-mounted pressure wave gauges, a bottom-mounted ADV, optical bottom-mounted pole wave gauges, and drone imagery.

2.1. Stereo Imaging System

A long-range, high-resolution two-camera stereo imaging system was specifically developed for this study. A pair of 5MP, global shutter CMOS digital cameras (Victorem 51B163-CX, IO Industries) were each fitted with a EF 200 mm f/2.8 L lens. The two cameras were placed on the ridge overlooking the beach, at a distance of 35 m from one another. The cameras were focused on a portion of water surface within the surf zone, located at a distance of approximately 150 m from the cameras. They were triggered simultaneously by a computer-controlled function generator (National Instruments PCIe 6612). A sketch of the instrument set-up is provided in Figure 1. Stereo observations of the sea surface have been used previously with the purpose of describing wave motion offshore and in the surf zone (see Benetazzo, 2006; Benetazzo et al., 2012; Bergamasco et al., 2017; de Vries et al., 2011 and references therein). Here, the cameras are used primarily for locating the orange tracers which simplifies the data analysis.

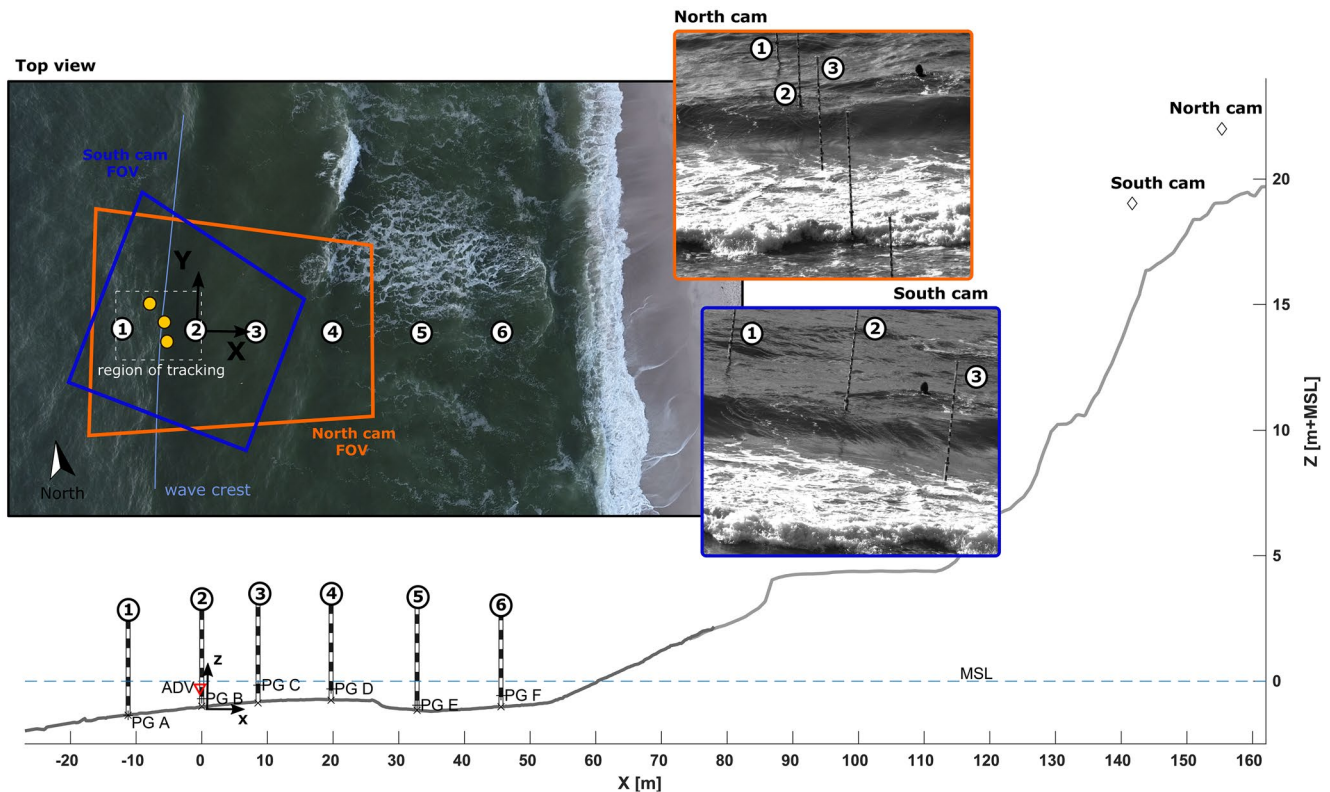


Figure 1. Experimental set-up: Six wave staffs were lined up in the direction of the incoming wavefield. Two cameras (North cam and South cam) were mounted on solid foundations atop dunes overlooking the beach. The two fields of view overlapped in a region including the first three wave staffs. Pressure sensors were mounted near the base of each pole. An acoustic Doppler velocimeter was mounted at the sea bed near Pole 2.

2.2. Supporting Measurements

Six graduated aluminum poles were jettied into the sand of an intertidal sandbar at low tide. The array of poles was delineated at an angle of about 281° which made them approximately perpendicular to the crests of incoming waves, although there were some slight variations in the angles of the wave crests. The most seaward pole (Pole 1) was about 80 m from the shore, and the closest pole (Pole 6) was about 20 m from the shoreline. At the base of each pole, a pressure gauge measured absolute pressure at 10 Hz sampling frequency. The recorded pressure signal was subdivided into 7–10 min data bursts and then transformed to surface excursion using the nonlinear, weakly dispersive method described in Bonneton et al. (2018) (see also Mouragues et al., 2019). Since the graduated poles were within the field of view of the stereo cameras (acquiring at 30 frames/s), these were also used as optical wave gauges.

At Pole 2, an upward looking, 6 MHz Nortek Vector ADV was deployed and measured Eulerian flow velocities at a sampling rate of 64 Hz. The elevation of the sensors with respect to the local datum as well the beach profile in the intertidal region was measured using an RTK-PDGPS. The elevation of the dry beach was extracted from photogrammetric digital elevation model, that was computed from airborne drone imagery using a DJI Matrice 210 RTK quadcopter.

2.3. Experimental Procedure

Oranges were deployed by a swimmer near Pole 1. These tracers are slightly buoyant, so that they always stayed at the free surface, and were well visible in the image frames. Images were acquired at 30 frames/s from both cameras. The data used in this article were acquired between 17:00 and 17:30 UTC on the seventh of September, 2019. The sea state was characterized by records from a buoy moored 1 km offshore in depth of 10 m which showed 1 m significant wave height and 7 s peak period. The incoming wavefield had a peak direction of 284.17° , and the mean wind speed was approximately 5 m/s from NNW.

2.4. Data Analysis

To obtain the intrinsic and extrinsic parameters for the two 200 mm cameras, a stereo camera calibration was conducted with the Matlab toolbox Stereo Camera Calibrator. The calibration result was validated with distances estimated using both pole graduations and the stereo imaging system. The root mean-squared difference for time series at Pole 1 obtained by pole graduation and by the stereo camera system is found to be less than 0.015 m.

Pairs of individual frames from camera footage were examined visually, and orange positions were recorded. A triangulation with the input of the stored pixel positions together with the calibration parameters was then done to construct 3D world-coordinate points. In order to create an appropriate coordinate system, a reasonable assumption is to assume that the crests are perpendicular to the line of poles such as indicated in Figure 1. A horizontal vector was found by using two known GPS-positions at Pole 2 and Pole 3, and with this a vertical vector along Pole 2 was found. With the described vectors, a 3D coordinate system can be created where the origin is placed at the bottom of Pole 2, the x -axis is pointing along the poles toward the beach, the y -axis is pointing along the wave crests and the z -axis is pointing upwards. With the three orthogonal basis vectors, the orange positions are placed in the described coordinate system and then projected onto the xz -plane.

Several Lagrangian trajectories are plotted together with free-surface elevation at the nearest wave pole in Figure 2. The full three-dimensional paths are plotted in the right panel, but for the purpose of analyzing the cross-shore movement, these paths are projected into the xz -plane. The wave height of the waves can be gauged from the left panel of Figure 2. For example for the wave indicated with blue, the wave height is $H = 0.48$ m. Since the distance between the poles is known, the wavelength can be calculated from the phase velocity and period to be 21.2 m. For the wave indicated in red, the wave height is $H = 0.35$ m, and the wavelength is 17.6 m. From Figure 2, it can be seen that the particle drift during one wave cycle is strongly correlated to the mean-water level in one wave. Indeed, the wave colored in green has a slight set-down, that is, the mean level is $\bar{\eta}_0 = -0.014$ m, and the net horizontal displacement of the tracer as shown in the right panel of Figure 2 is -0.30 m. For the blue wave, the mean level is $\bar{\eta}_0 = 0.117$ m, and the net cross-shore displacement is 1.23 m. Similarly, the red wave features a negative mean level and a negative net displacement while the yellow wave features a positive mean level and a positive net displacement. The relation between mean-water level and net drift will be quantified using a complete wave record below. In the lower left panel of Figure 2 in addition to the main spectral peaks at 6.18, 4.92, and 3.95 s, two smaller spectral peaks at 28.6 and 13.8 s are also visible. The 28.6 s peak is clearly related to wave group behavior. A representative 5-min window of the wave record is shown in the lower right panel of Figure 2. The wave group structure is visible but somewhat irregular. For wave groups, it is expected from theoretical studies and laboratory experiments (Calvert et al., 2019; Longuet-Higgins & Stewart, 1962) that the wave envelope has the property that troughs are approximately aligned with the peaks of the mean-water level and peaks are approximately aligned with the troughs of the mean-water level. In the record shown, the wave envelope (shown in solid blue) and the low-passed wavefield (shown in black) are negatively correlated as expected, but the correlation is weak at -0.401 . This indicates that some of the infragravity wave signal is still due to bound waves, but reflected waves and waves created in the surf zone are also present.

3. Discussion

In the present work, Lagrangian particle paths in individual waves in the surf zone were recorded. As shown in the previous section, the data acquisition methods and data processing procedures utilized in this study resulted in highly accurate measurements of the tracer positions. In order to better understand the observed in situ particle paths, comparisons with a theoretical wave model were performed. At present, only the cross-shore movement is analyzed, and the data points are projected as described above.

Typical wavelengths λ in the data sets considered here are in the range from 10 m to about 40 m, and wave heights H for nonbreaking waves range from 0.2 m to about 1 m, though as can be seen in the upper left panel in Figure 4, most nonbreaking waves in the record considered there have a wave height below 0.7 m. Given that the local water depth h_0 was on the order of 2 m, the Ursell number defined by $\mathcal{U} = H\lambda^2/h_0^3$ at

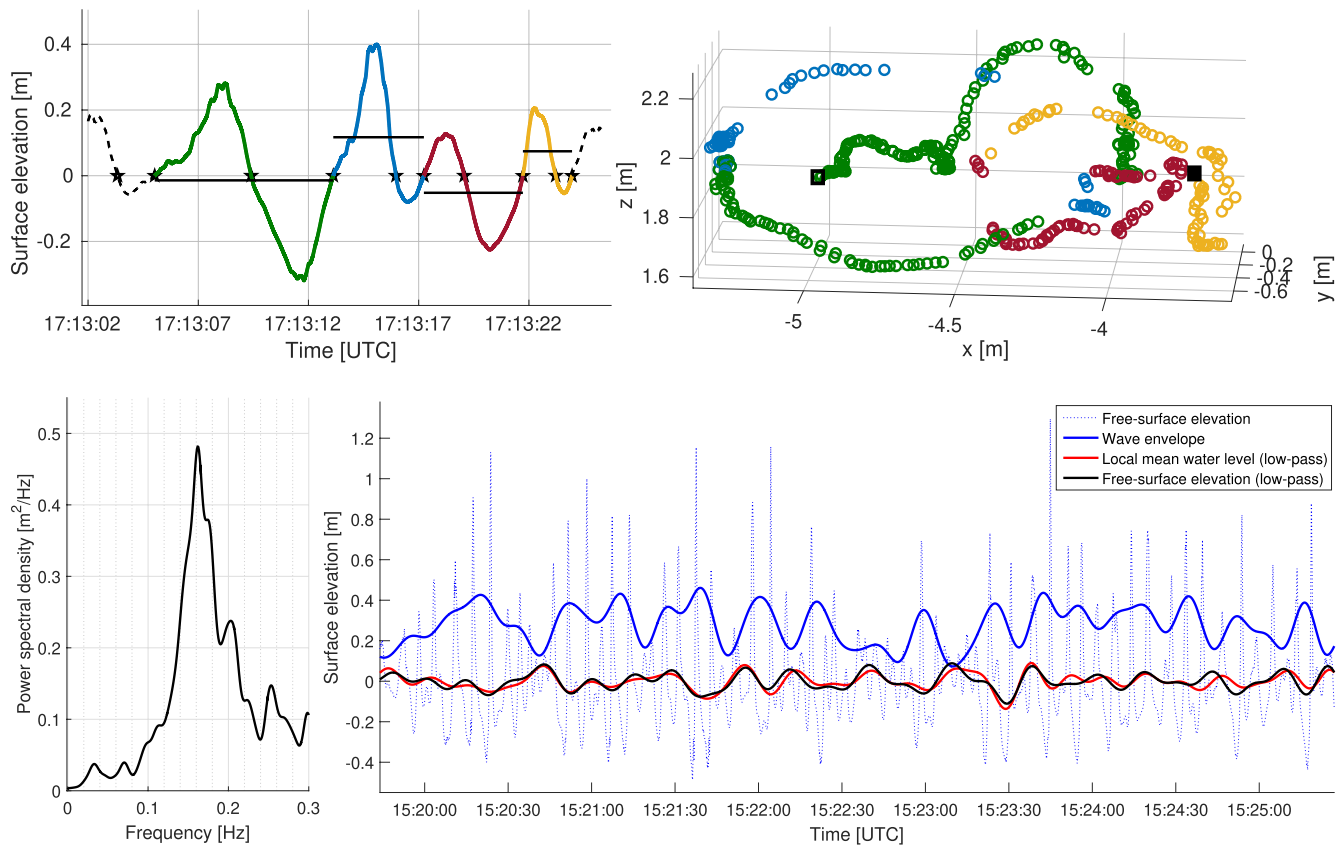


Figure 2. Upper left: time series of free-surface elevation for nonbreaking waves. The surface excursion is reconstructed from pressure data collected by pressure gauge mounted at the base of Pole 2. The black lines represent the average of the free-surface elevation over the zero-crossing period. Upper right: Lagrangian motion of a particle tracer in the same time window as the free-surface data in the left panel. The blue and yellow waves feature instantaneous wave set-up and corresponding strong shoreward Lagrangian transport while the red wave features set-down and backward drift. The black rectangle indicates the tracer position when tracking commenced, and the solid black square indicates the final tracer position. There are some gaps in the tracer positions in cases when the tracer was not visible in both cameras. Due to inherent differences between Eulerian and Lagrangian measurements as well as tracer drift, there are slight differences in the observed wave height between the upper left and upper right panels. Lower left: The power spectral density as a function of frequency. Lower right: The blue-dashed curve is the free-surface elevation calculated from the pressure data measured by pressure gauge mounted at Pole 1 and with a low-pass Butterworth filter with a cutoff frequency of 0.075 Hz, the free-surface elevation is plotted as the black curve. The red curve represents the local mean-water level obtained by zero-crossing analysis and the blue solid curve shows the wave envelope computed using the Hilbert transform (Janssen et al., 2003).

the measurement location is generally larger than 5, and for such values, nonlinear theory should be used (Dingemans, 1997). There are many numerical models used in coastal modeling of shoaling waves, most of which use some form of the Boussinesq equations (see, e.g., Roeber et al., 2010). In the present case, we are interested in particle motion and orbital velocities in the fluid at a fixed site and for waves traveling toward the shore, and we therefore choose the Korteweg-de Vries (KdV) equation

$$\eta_t + \left(c_0 + \frac{3}{2} \frac{c_0}{h_0} \eta \right) \eta_x + \frac{1}{6} c_0 h_0^2 \eta_{xxx} = 0, \quad (1)$$

where h_0 is the local water depth, and $c_0 = \sqrt{gh_0}$ is the limiting long-wave speed. This equation is the simplest nonlinear shallow-water equation which also incorporates dispersive effects. Assuming long-crested waves, a cross-section (such as along the measurement poles) of the free surface can be expressed for one period as

$$\eta(x, t) = f_2 - (f_2 - f_1) \text{cn}^2 \left(2K(m) \left(\frac{t}{T} - \frac{x}{\lambda} \right), m \right), \quad (2)$$

where cn is a Jacobian elliptic function, f_1 , f_2 , and f_3 are three parameters that can be chosen arbitrarily, m is the elliptic modulus defined by $m = \frac{f_1 - f_2}{f_1 - f_3}$, and $K(m)$ and $E(m)$ are the complete elliptic integrals of the first and second kind [Lawden, 2013]. The wave speed c , the wavelength λ , and period T are then given by

$$c = c_0 \left(1 + \frac{f_1 + f_2 + f_3}{2h_0} \right), \quad \lambda = K(m) \sqrt{\frac{16h_0^3}{3(f_1 - f_3)}}, \quad T = \lambda/c. \quad (3)$$

In order to use these formulas in the current context to fit the wave-by-wave particle paths, it is convenient to take the wave height H , the mean surface level $\bar{\eta}_0$, and the elliptic parameter m as the defining parameters. These are related to f_1 , f_2 , and f_3 via the equations

$$f_3 = \bar{\eta}_0 - \frac{HE(m)}{mK(m)}, \quad f_1 = f_3 + \frac{H}{m}, \quad f_2 = f_1 - H. \quad (4)$$

This representation may be found in Dingemans (1997) for the case $\bar{\eta}_0 = 0$. Due to the oscillations of the mean-water level, it is essential in the present context to allow for nonzero $\bar{\eta}_0$. Note that the depth h_0 also appears in Equation 3, but can be removed by dimensional analysis. The procedure used to obtain compare the tracer data with the KdV theory can be summarized as follows. First, individual waves are identified using a zero-crossing segmentation of the wavefield based on the tracer positions. Since the wave height is known from the tracer data, we have to fit the two remaining parameters m and $\bar{\eta}_0$. In order to fit these parameters, we first need to compute particle paths associated with Equation 2. Taking the functions $\xi(t)$ and $\zeta(t)$ to describe the x -coordinate and z -coordinate, respectively, of a particle originally located at a point $(x, z) = (\xi_0, \zeta_0)$ given from the tracer position, the particle motion is described by the differential equations

$$\frac{\partial \xi}{\partial t} = u(\xi(t), \zeta(t), t), \quad \frac{\partial \zeta}{\partial t} = v(\xi(t), \zeta(t), t), \quad (5)$$

with initial conditions $\xi(0) = \xi_0$ and $\zeta(0) = \zeta_0$. As shown in Borluk and Kalisch (2012), the velocity field u, v can be written in terms of the free-surface excursion η and various derivatives, and these equations can be solved numerically. The optimal parameters m and $\bar{\eta}_0$ are then found by minimizing the error between the tracer positions and the numerical simulations of the particle paths.

One feature which is clearly brought out by the black average bars in the upper left panel of Figure 2 and the mean-water level $\bar{\eta}_0$ computed for the waves shown in Figure 3 (left) is that strong forward transport coincides with elevated mean-water level. In addition, the numerical approximations of particle paths further down in the fluid column shown in Figure 3, suggest that the local mean-water level affects transport properties not only near the free surface, but also farther down in the fluid column. Indeed, the two cases shown in Figure 3, clearly show the difference in average horizontal velocities for a wave with set-down, and a wave with set-up. The large particle drift at all depths which can be seen in the numerical simulations of the wave with positive set-up (lower left panel of Figure 3) is a clear departure from the case of a breaking or pre-breaking wave which features strong forward transport near the free surface. Indeed, it has been observed in wave flume experiments and numerical simulations that wave breaking induces a slight backward drift at depths about halfway down from the surface (Deike et al., 2017; Harms & Schlurmann, 2005).

In order to ensure that this strong mass transport throughout the fluid column is not a theoretical artifact, we analyzed data from ADV current measurements which are about 1 m below the free surface. Usually, ADV measurements are taken near the bottom in order to study sediment transport and undertow. In the present case, the ADV was pointing upwards in order to capture the flow velocity in the center of the fluid column.

As mentioned above, time series of the free surface at Poles 1, 2, and 3 were reconstructed from pressure gauge data using a nonlinear weakly dispersive approximation introduced in Bonneton et al. (2018) and termed SNL (shallow nonlinear) approximation. Waves which were breaking or close to breaking were identified by visual inspection and flagged for possible exclusion. Data based on a representative 7 – 1/2-min wave record are evaluated in Figure 4. As indicated by the scatter plot relating wave-by-wave mean-water level and forward transport in Figure 4, the correlation between average Eulerian velocity \bar{u}_E during one wave period and mean-water level $\bar{\eta}_0$ is strong. In contrast, the correlation between the average Eulerian velocity and the wave height H is weak. These numbers are nearly unchanged if breaking waves are excluded from the computations. The upper right panel of Figure 4 shows the correlation between wave-by-wave mean-water level and average Lagrangian drift \bar{u}_L during one wave period. The strong correlation of about 0.75 between $\bar{\eta}_0$ and \bar{u}_E represents quantitative confirmation of the dependence of the mass transport in the fluid column on the local mean-water level which was indicated in Figure 3 for a particular case.

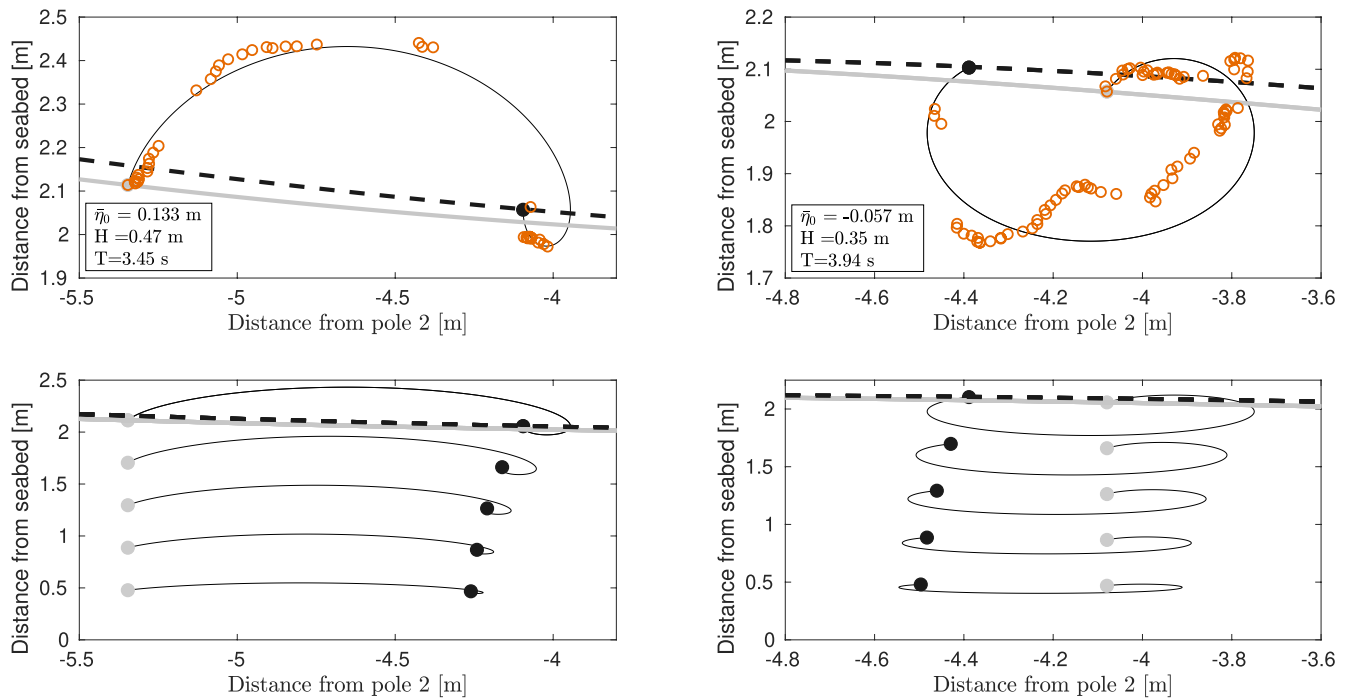


Figure 3. Comparison between measured particle trajectories using buoyant tracers, and particle trajectories in the nonlinear KdV approximation for the blue wave (left panels) and red wave (right panels) from Figure 2. The orange circles indicate the measured tracer positions. The thin black solid lines represent numerically computed particle paths with the gray dot representing the initial tracer position used in the comparison, and the black dot representing the final computed particle position. The gray thick lines represent the free surface in the KdV approximation at the start of the comparison, and the black dashed lines represent the free surface in the KdV approximation at the final time. Strong net shoreward transport throughout the fluid column is observed in the left panel while slight seaward transport is observed in the right panel.

It is clear from the analysis provided here that short-term oscillations in the wave set-up may constitute a significant factor in shoreward mass transport. In contrast, the wave heights of the individual waves were not found to be a good indicator of shoreward mass transport either at the free surface or otherwise.

In addition to affecting shoreward mass transport, it is possible that the observed oscillations of the mean-water level also constitute a mechanism for infragravity wave dissipation as the higher orbital velocities may facilitate wave breaking in waves with relatively smaller wave height and wave celerity. Infragravity wave dissipation may be attributed to bottom friction, transfer of energy to shorter waves through quadratic coupling, direct infragravity wave self-interaction resulting in steepening and the eventual breaking and bore formation (Battjes et al., 2004; De Bakker, Tissier, & Ruessink, 2016; Rijnsdorp et al., 2015; Van Dongeren et al., 2007).

The close correlation between Lagrangian velocities at the free surface and oscillations of the mean-water level observed here suggest that dissipation of infragravity waves may also be achieved by gravity-wave breaking and subsequent smearing out of the infragravity wavefield by broken shorter waves. Indeed, the increased Lagrangian velocity at the free surface can be easily seen to facilitate short-wave breaking in view of the kinematic criterion for wave breaking (see Itay & Liberzon, 2017, Hatland & Kalisch, 2019 and references therein). Unfortunately, the size of the FOV of the stereo camera system and the length of the array of wave poles and PG did not provide spatial extent to test this hypothesis. In fact, decay and reflection of infragravity waves is highly dependent on environmental characteristics such as beach slope, sand bar structure, and many other factors (Bertin et al., 2018), and a precise understanding of this hypothesis will require future field campaigns on a variety of beach profiles and wave conditions as well as laboratory experiments.

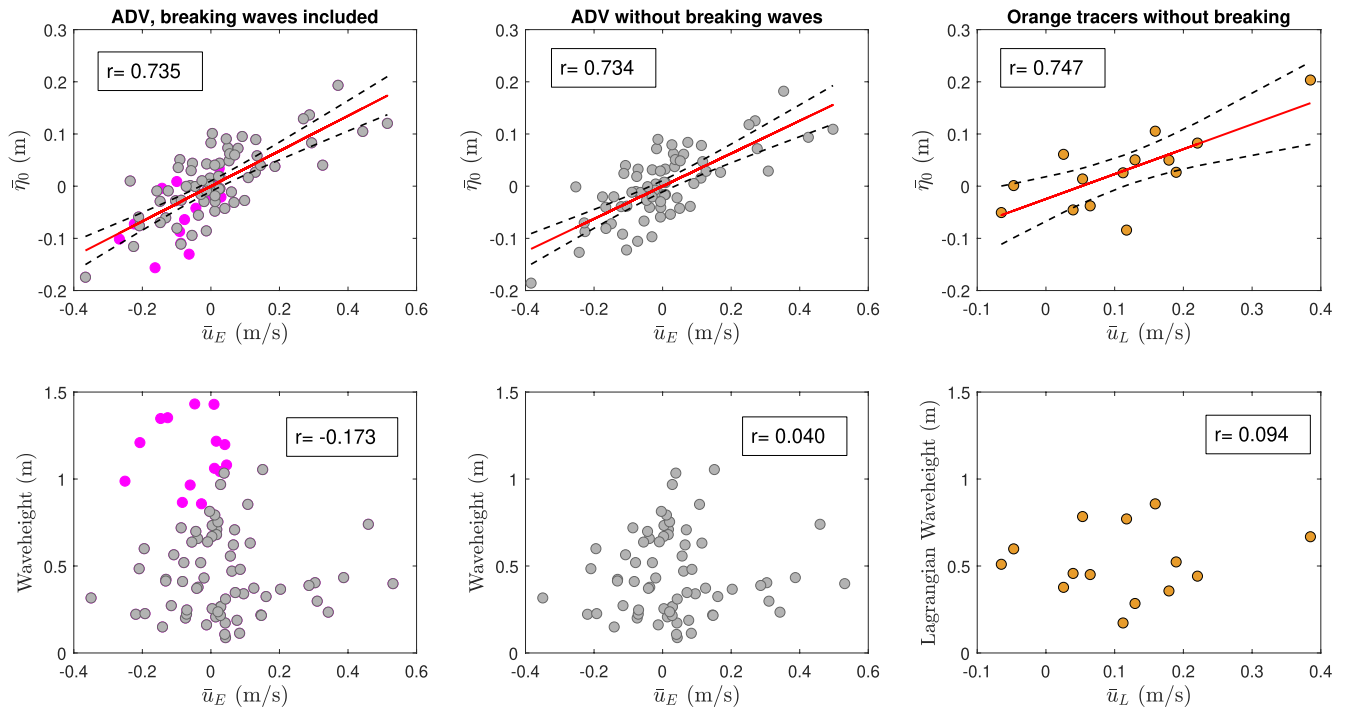


Figure 4. Upper panels: correlation between wave-by-wave values of mean free-surface elevation $\bar{\eta}_0$ and mean Eulerian velocity including breaking waves (left, $r = 0.735$), mean Eulerian velocity exclusive of breaking waves (center $r = 0.734$), mean Lagrangian velocity at the free surface (right $r = 0.747$). The red lines are the regression lines and the black dotted curves show the 95% confidence interval for the regression line estimate. Lower panels: correlation between wave height and mean Eulerian velocity including breaking waves (left), mean Eulerian velocity exclusive of breaking waves (center), mean Lagrangian velocity at the free surface (right). Gray dots indicate Eulerian measurements in nonbreaking waves, magenta dots indicate Eulerian measurements in waves which are spilling or breaking. Orange dots indicate Lagrangian measurements of orange tracers at the free surface (nonbreaking).

Data Availability Statement

Wave buoy data and data of particle trajectories acquired during this study are available for public access at <https://zenodo.org/record/5211265>.

References

- Battjes, J., Bakkenes, H., Janssen, T., & van Dongeren, A. R. (2004). Shoaling of subharmonic gravity waves. *Journal of Geophysical Research*, *109*(C2). <https://doi.org/10.1029/2003jc001863>
- Benetazzo, A. (2006). Measurements of short water waves using stereo matched image sequences. *Coastal Engineering*, *53*(12), 1013–1032. <https://doi.org/10.1016/j.coastaleng.2006.06.012>
- Benetazzo, A., Fedele, F., Gallego, G., Shih, P.-C., & Yezzi, A. (2012). Offshore stereo measurements of gravity waves. *Coastal Engineering*, *64*, 127–138. <https://doi.org/10.1016/j.coastaleng.2012.01.007>
- Bergamasco, F., Torsello, A., Scavo, M., Barbariol, F., & Benetazzo, A. (2017). Wass: An open-source pipeline for 3d stereo reconstruction of ocean waves. *Computers & Geosciences*, *107*, 28–36. <https://doi.org/10.1016/j.cageo.2017.07.001>
- Bertin, X., De Bakker, A., Van Dongeren, A., Coco, G., Andre, G., Arduin, F., et al. (2018). Infragravity waves: From driving mechanisms to impacts. *Earth-Science Reviews*, *177*, 774–799. <https://doi.org/10.1016/j.earscirev.2018.01.002>
- Bonneton, P., Lannes, D., Martins, K., & Michallet, H. (2018). A nonlinear weakly dispersive method for recovering the elevation of irrotational surface waves from pressure measurements. *Coastal Engineering*, *138*, 1–8. <https://doi.org/10.1016/j.coastaleng.2018.04.005>
- Borluk, H., & Kalisch, H. (2012). Particle dynamics in the KDV approximation. *Wave Motion*, *49*(8), 691–709. <https://doi.org/10.1016/j.wavemoti.2012.04.007>
- Buckley, M. L., Lowe, R. J., Hansen, J. E., van Dongeren, A. R., & Storlazzi, C. D. (2018). Mechanisms of wave-driven water level variability on reef-fringed coastlines. *Journal of Geophysical Research: Oceans*, *123*(5), 3811–3831. <https://doi.org/10.1029/2018jc013933>
- Calvert, R., Whittaker, C., Raby, A., Taylor, P. H., Borthwick, A., & Van Den Bremer, T. (2019). Laboratory study of the wave-induced mean flow and set-down in unidirectional surface gravity wave packets on finite water depth. *Physical Review Fluids*, *4*(11), 114801. <https://doi.org/10.1103/physrevfluids.4.114801>
- Castelle, B., Scott, T., Brander, R., & McCarroll, R. (2016). Rip current types, circulation and hazards. *Earth-Science Reviews*, *163*, 1–21. <https://doi.org/10.1016/j.earscirev.2016.09.008>
- Chen, Y.-Y., Hsu, H.-C., & Chen, G.-Y. (2010). Lagrangian experiment and solution for irrotational finite-amplitude progressive gravity waves at uniform depth. *Fluid Dynamics Research*, *42*(4), 045511. <https://doi.org/10.1088/0169-5983/42/4/045511>
- Davidson-Armott, R., Bauer, B., & Houser, C. (2019). *Introduction to coastal processes and geomorphology*. Cambridge University Press.

Acknowledgments

The authors thank J. Bödewadt, J. Stell, and L. Zorn for technical support. The authors acknowledge funding from the Research Council of Norway under grant no. 239033/F20, from the Coasts in the Changing Earth System (PACES II) program of the Helmholtz Association, and support from the Deutsche Forschungsgemeinschaft (DFG, German Research Foundation, project number 274762653, Collaborative Research Centre TRR 181 *Energy Transfers in Atmosphere and Ocean*). The authors would also like to thank two anonymous reviewers whose constructive criticism helped us improve the paper significantly.

- De Bakker, A., Brinkkemper, J., Van der Steen, F., Tissier, M., & Ruessink, B. (2016). Cross-shore sand transport by infragravity waves as a function of beach steepness. *Journal of Geophysical Research: Earth Surface*, 121(10), 1786–1799. <https://doi.org/10.1002/2016jf003878>
- De Bakker, A., Tissier, M., & Ruessink, B. (2016). Beach steepness effects on nonlinear infragravity-wave interactions: A numerical study. *Journal of Geophysical Research: Oceans*, 121(1), 554–570. <https://doi.org/10.1002/2015jc011268>
- Deike, L., Pizzo, N., & Melville, W. K. (2017). Lagrangian transport by breaking surface waves. *Journal of Fluid Mechanics*, 829, 364–391. <https://doi.org/10.1017/jfm.2017.548>
- de Vries, S., Hill, D., De Schipper, M., & Stive, M. (2011). Remote sensing of surf zone waves using stereo imaging. *Coastal Engineering*, 58(3), 239–250. <https://doi.org/10.1016/j.coastaleng.2010.10.004>
- Dingemans, M. W. (1997). *Water wave propagation over uneven bottoms* (Vol. 13). World Scientific.
- Elgar, S., & Raubenheimer, B. (2020). Field evidence of inverse energy cascades in the surfzone. *Journal of Physical Oceanography*, 50(8), 2315–2321. <https://doi.org/10.1175/jpo-d-19-0327.1>
- Harms, J., & Schlurmann, T. (2005). Time-variant mass transport beneath breaking waves. In *Coastal engineering 2004: (in 4 volumes)* (pp. 441–453). World Scientific. https://doi.org/10.1142/9789812701916_0034
- Hatland, S. D., & Kalisch, H. (2019). Wave breaking in undular bores generated by a moving weir. *Physics of Fluids*, 31(3), 033601. <https://doi.org/10.1063/1.5085861>
- Inch, K., Davidson, M., Masselink, G., & Russell, P. (2017). Observations of nearshore infragravity wave dynamics under high energy swell and wind-wave conditions. *Continental Shelf Research*, 138, 19–31. <https://doi.org/10.1016/j.csr.2017.02.010>
- Inman, D. L., & Brush, B. M. (1973). The coastal challenge. *Science*, 181(4094), 20–32. <https://doi.org/10.1126/science.181.4094.20>
- Itay, U., & Liberzon, D. (2017). Lagrangian kinematic criterion for the breaking of shoaling waves. *Journal of Physical Oceanography*, 47(4), 827–833. <https://doi.org/10.1175/jpo-d-16-0289.1>
- Janssen, T., Battjes, J., & Van Dongeren, A. (2003). Long waves induced by short-wave groups over a sloping bottom. *Journal of Geophysical Research*, 108(C8). <https://doi.org/10.1029/2002jc001515>
- Lawden, D. F. (2013). *Elliptic functions and applications* (Vol. 80). Springer Science & Business Media.
- Lin, Y.-H., & Hwung, H.-H. (2012). Infra-gravity wave generation by the shoaling wave groups over beaches. *China Ocean Engineering*, 26(1), 1–18. <https://doi.org/10.1007/s13344-012-0001-9>
- List, J. H. (1992). A model for the generation of two-dimensional surf beat. *Journal of Geophysical Research*, 97(C4), 5623–5635. <https://doi.org/10.1029/91jc03147>
- Longuet-Higgins, M. S., & Stewart, R. (1962). Radiation stress and mass transport in gravity waves, with application to surf beats. *Journal of Fluid Mechanics*, 13(4), 481–504. <https://doi.org/10.1017/s00222112062000877>
- Longuet-Higgins, M. S., & Stewart, R. (1964). Radiation stresses in water waves; a physical discussion, with applications. In *Deep Sea Research and Oceanographic Abstracts* (Vol. 11, pp. 529–562). [https://doi.org/10.1016/0011-7471\(64\)90001-4](https://doi.org/10.1016/0011-7471(64)90001-4)
- Masselink, G. (1995). Group bound long waves as a source of infragravity energy in the surf zone. *Continental Shelf Research*, 15(13), 1525–1547. [https://doi.org/10.1016/0278-4343\(95\)00037-2](https://doi.org/10.1016/0278-4343(95)00037-2)
- Masselink, G., Hughes, M., & Knight, J. (2014). *Introduction to coastal processes and geomorphology*. Routledge.
- Mouragues, A., Bonneton, P., Lannes, D., Castelle, B., & Mariu, V. (2019). Field data-based evaluation of methods for recovering surface wave elevation from pressure measurements. *Coastal Engineering*, 150, 147–159. <https://doi.org/10.1016/j.coastaleng.2019.04.006>
- Putrevu, U., & Svendsen, I. A. (1999). Three-dimensional dispersion of momentum in wave-induced nearshore currents. *European Journal of Mechanics - B: Fluids*, 18(3), 409–427. [https://doi.org/10.1016/s0997-7546\(99\)80038-7](https://doi.org/10.1016/s0997-7546(99)80038-7)
- Rijnsdorp, D. P., Ruessink, G., & Zijlema, M. (2015). Infragravity-wave dynamics in a barred coastal region, a numerical study. *Journal of Geophysical Research: Oceans*, 120(6), 4068–4089. <https://doi.org/10.1002/2014jc010450>
- Roeder, V., Cheung, K. F., & Kobayashi, M. H. (2010). Shock-capturing Boussinesq-type model for nearshore wave processes. *Coastal Engineering*, 57(4), 407–423. <https://doi.org/10.1016/j.coastaleng.2009.11.007>
- Russell, P. E. (1993). Mechanisms for beach erosion during storms. *Continental Shelf Research*, 13(11), 1243–1265. [https://doi.org/10.1016/0278-4343\(93\)90051-x](https://doi.org/10.1016/0278-4343(93)90051-x)
- Sharifi, M., Rafiee, S., Keyhani, A., Jafari, A., Mobli, H., Rajabipour, A., & Akram, A. (2007). Some physical properties of orange [var. Tompson]. *International Agrophysics*, 21(4), 391–397.
- Svendsen, I. A. (2006). *Introduction to nearshore hydrodynamics* (Vol. 24). World Scientific.
- Tucker, M. (1950). Surf beats: Sea waves of 1 to 5 min. period. *Proceedings of the Royal Society of London—Series A: Mathematical and Physical Sciences*, 202(1071), 565–573.
- Umeyama, M. (2012). Eulerian-Lagrangian analysis for particle velocities and trajectories in a pure wave motion using particle image velocimetry. *Philosophical Transactions of the Royal Society A: Mathematical, Physical & Engineering Sciences*, 370(1964), 1687–1702. <https://doi.org/10.1098/rsta.2011.0450>
- Van Dongeren, A., Battjes, J., Janssen, T., Van Noorloos, J., Steenhauer, K., Steenbergen, G., & Reniers, A. (2007). Shoaling and shoreline dissipation of low-frequency waves. *Journal of Geophysical Research*, 112(C2). <https://doi.org/10.1029/2006jc003701>
- van Thiel de Vries, J. S. M., Van Gent, M., Walstra, D., & Reniers, A. (2008). Analysis of dune erosion processes in large-scale flume experiments. *Coastal Engineering*, 55(12), 1028–1040. <https://doi.org/10.1016/j.coastaleng.2008.04.004>